A Fully Integrated Common-Mode Choke Design Embedded With Differential-Mode Capacitances

Shiqi Jiang, *Graduate Student Member, IEEE*, Wei Wang, *Member, IEEE*, Panbao Wang, *Senior Member, IEEE*, and Dianguo Xu, *Fellow, IEEE*

***Abstract*—The emerging flexible multilayer foils (FMLFs)-based winding design has a great potential to promote the magnetic integration technique in power electronic systems. This article investigates the full integration of a single-phase electromagnetic interference (EMI) choke with well-designed FMLFs. By sharing a UU-type core and configuring the windings reasonably, all the common-mode (CM) inductance and capacitances and differential-mode (DM) inductances and capacitances can be integrated into the same core unit. Moreover, the proper terminal configuration of conductive layers can realize function-decoupling between CM and DM filtering elements, which contributes to simplifying the equivalent CM and DM models, then predigesting the parameters design procedure. Following the modeling and theoretical analysis, prototypes of the proposed and existing EMI chokes have been built for a single-phase 200-kHz SiC-MOSFET inverter system. Through experimental measurements, performance comparisons have been presented to demonstrate the validity of this model.**

***Index Terms*—Common mode (CM), differential mode (DM), electromagnetic interference (EMI), EMI choke, flexible multilayer foils (FMLFs), full integration, function decoupling.**

I. Introduction

POWER converter systems (PCSs) are widely utilized in aerospace, medical instruments, new energy generation system, and other important application fields that with high-reliability requirements [1]–[3]. Nevertheless, on account of the high-speed switching operation, PCSs are potential sources of relevant electromagnetic interference (EMI) for themselves and electric equipment placed nearby. These EMI emissions will interfere with the normal operation of the equipment, shorten its service life and pollute the associated environment [4], [5]. Therefore, limiting the EMI noise under a reliable level is necessary for a PCS. There are some authoritative standards that should be met for PCSs in different applications, such as EN55011-Class A and Class-B [6], which provide a required design objective of electromagnetic compatibility for the system. Moreover, with the development of PCSs to high frequency and high power-density, it is a great challenge to solve the EMI issue with a promotion to the development.

Various strategies have been proposed to response to the challenge that referred to above from different perspectives; they can be classified into two categories: 1) indirect and 2) direct methods. Indirect methods like soft-switching [7], advanced pulsewidth modulation techniques [8], [9], rectifying the layout of the circuit [10], and improving the topologies of PCSs [11], [12] are aimed at reducing the consumption of passive filtering elements by mitigating the original EMI level in the target system. Although these methods can degrade the EMI noise source, relevant conducted EMI noise is still hard to be reduced to meet the requirements only through these improvements. Thus, indirect methods are generally applied to play auxiliary roles for EMI mitigation [13]. In contrast, the direct approaches represented by designing EMI filters usually take leading roles. There are two types of EMI filters, 1) active and 2) passive. The effectiveness of an active EMI filter is highly dependent on the high-frequency performance of constituent modules, especially the sensor part [14], [15]. Although active EMI filters are superior in integration design, their insertion losses (ILs) are commonly unsatisfactory in the high-frequency range due to stray parameters of the components. Compared with active EMI filters, passive EMI filters are more widely adopted in industrial applications because of their better stability and reliability [16]. A passive EMI filter is generally composed of common-mode (CM) and differential-mode (DM) filtering modules; it is one of the main parts of the output filter in a PCS. However, the utilization of the traditional passive EMI filters will bring in more discrete electromagnetic components, which will significantly enlarge the weight and size of the system. Therefore, developing and optimizing the integration design of passive EMI filters has a far-reaching impact on promoting their future applications in different fields.

As the most representative approach, the magnetic integration technique has been being developed and updated constantly. It is well known that the traditional magnetic integration techniques are focused on the integration design of several magnetic components in different modes or with different functions. Its application in the EMI filter design has been investigated in depth. In [17], a relatively low-permeability DM choke is placed within the open window of the CM choke. Both chokes share the same winding structure for integrating CM and DM inductors

Manuscript received July 22, 2021; revised October 14, 2021; accepted November 28, 2021. Date of publication December 2, 2021; date of current version January 19, 2022. This work was supported in part by the Natural Science Foundation of China under Grant 51977045 and in part by the Power Electronics Science and Education Development Program of Delta Group under Grant DREG2020009. Recommended for publication by Associate Editor G. Oriti. *(Corresponding author: Panbao Wang.)*

The authors are with the School of Electrical Engineering and Automation, Harbin Institute of Technology, Harbin 150001, China (e-mail: jiangshiqi@hit.edu.cn; wangwei602@hit.edu.cn; wangpanbao@hit.edu.cn; xudiang@hit.edu.cn).

Color versions of one or more figures in this article are available at https://doi.org/10.1109/TPEL.2021.3132035.

Digital Object Identifier 10.1109/TPEL.2021.3132035

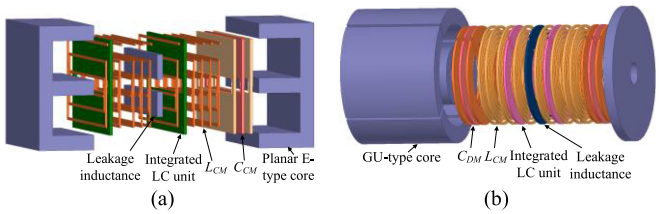

Fig. 1. Typical planar integrated structures of EMI filters based on (a) EE-type and (b) GU-type cores.

onto one built-up core. In [18], a step-by-step design method of magnetic integrated single- and multistage EMI filters with EE/EIE-type cores have been introduced, which provides a comprehensive integration design idea. Recently, an EE-core-based integration scheme for the coupled inductor and DM inductances has been suggested for a paralleled inverter system with no CM noise attenuation requirement [19]. Indeed, this approach has superiority in the specific application, but meanwhile, its utilization has a great limitation. In [20], a novel integrated EMI choke that consists of a toroid and a solenoid has been presented. Similar to the model in [17], this structure properly utilizes the open window of the toroidal core, independent DM inductances can be designed in the integrated unit through an embedded solenoid with low permeability. In addition, some structures are designed to integrate both harmonic and EMI filtering inductors [21], [22]. These developing traditional magnetic integration techniques have a great contribution to promoting the integration design of magnetic components. But the integration level is still greatly constrained due to the unicity of the passive components that can be integrated. For seeking a breakthrough, planar integration techniques have been investigated following the traditional design concept. In [23], a planar-winding-based *LC* cell is presented and analyzed through the generalized transmission structure theory discussed in [24]. It provides a basic concept for the integration of a coil inductance and a parallel plate capacitance. With the expansion of planar integration methods, this new concept has been quickly introduced into the design of EMI filters and has been developed with various planar core and winding structures [25], [26]. Fig. 1 shows the typical planar integrated structures of EMI filters. In this way, in order to facilitate the integration design combined with the circuit board, the magnetic components tend to be designed with the printed circuit board (PCB) based windings. Although the PCB-winding-based planar magnetic components can significantly reduce the height of the PCS, it generally needs an extended PCB area, especially when it requires a great inductance. On the other hand, the emerging flexible multilayer foil (FMLF) techniques have provided a novel idea, which uses interleaved flexible copper foil and band-shaped dielectric materials to design windings for achieving electromagnetic integration. Compared with planar integration techniques, FMLF techniques are more flexible and convenient to realize different electrical configurations. Meanwhile, they can provide a more compact model to meet the design requirements. Moreover, the total length and area of the windings will be significantly reduced with FMLF techniques [27]. In [28], the basic principles of FMLF techniques for the EMI filter design are presented, and they have been further developed in [29], which derived various commonly used basic *LC* structures. Based on these fundamental models, the utilization of FMLF techniques can be expanded to the integration design of different passive components in various power electronic converters [30]. In [31] and [32], for reducing the size dominated by massive passive components in light-emitting diode (LED) drivers, the integrated passive devices for the required resonant inductor, transformer (one or two), and resonant capacitors (one or two) are proposed. Moreover, in addition to the components mentioned above, an integrated unit that extra contains a CM inductor is designed in [33] for a multichannel series resonant LED driver. Similar to these applications, FMLF integration techniques are introduced to the design of resonant converters [34]–[36], which aims at integrating the transformer, resonant module, and other capacitive or inductive components (boost inductor, output inductor, filtering inductor, and capacitors) if required. Following this train of thought, an FMLFs and PCB-winding-based passive integration structure is proposed in [37] for a Γ–Z source dual active bridge dc–ac bidirectional converter, which covers two filter capacitors, two boost inductors, two series resonant capacitors, two series resonant inductors, and two transformers. From these extended applications, it can be observed that FMLF techniques have a great capacity to promote the power integration design, but they still need to be further developed. As important parts of power converters, the filters with different functions can provide a vast space for the utilization of FMLF techniques. In terms of the design of the output filter and the EMI filter, a symmetrical *LC*-type harmonic filter and a CM choke have been fully integrated into [29] and [38], respectively. The model in [38] is made up of a UU-core and two single-strip FMLF-based windings, which is able to integrate both the CM inductance and capacitances. However, this model has no independent integrated DM filtering components, its DM attenuation ability is quite limited. It generally needs extra discrete DM filtering components to improve the DM attenuation performance, this is a major drawback. In addition, the single-strip FMLF winding will lead to many flux leakages, which may interfere with the near devices. Actually, FMLF techniques have a great potential to achieve both higher integration-level and modified performance with improved FMLFs structure.

For compensating for the shortcoming of the existing FMLF-based CM choke, in this article, extra DM capacitances are aimed to be integrated into the same unit. However, DM capacitance is generally much greater than the CM capacitance, using common single-strip windings will result in excessive material consumption. Hence, different from that in [38], two well-designed interleaved multistrip FMLF-based windings are utilized in this article for obtaining greater capacitances. Through the proper configuration of their terminals, the main capacitances generated by the windings can serve as DM capacitances. With this structure, the flux leakages of the winding will be significantly reduced, this can ameliorate the radiated emissions though the equivalent DM inductance will be decreased. But meanwhile, the integrated DM capacitors can upgrade the equivalent DM filtering circuit, thereby improving the DM attenuation on the whole. In addition, a GND layer with a required length is

TABLE I
EQUIVALENT MODELS OF THE COMMON USED FMLF WINDINGS UNDER DIFFERENT ACTIVATING MODES

Winding structure	Distributed model	Equivalent model of the winding under different activated modes		Parameter value
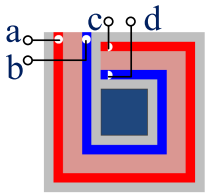 Single-strip FMLFs winding	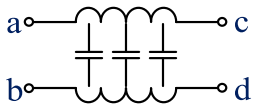	CN1	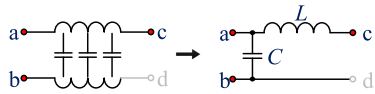	$L=N^2/R$ $C=\varepsilon_r\varepsilon_0 A/d$
		CN2	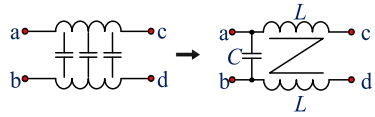	$L=2N^2/R$ $C=\varepsilon_r\varepsilon_0 A/d$
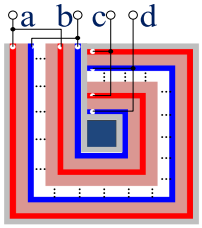 Multi (n)-strip FMLFs winding	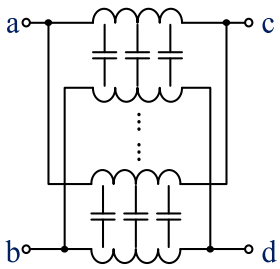	CN1	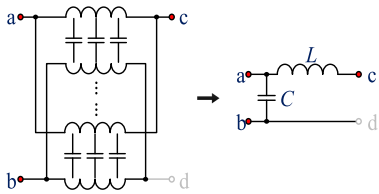	$L=N^2/R$ $C=(2n\text{-}1)\varepsilon_r\varepsilon_0 A/d$
		CN2	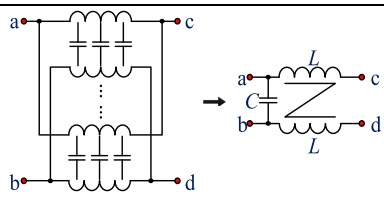	$L=2N^2/R$ $C=(2n\text{-}1)\varepsilon_r\varepsilon_0 A/d$

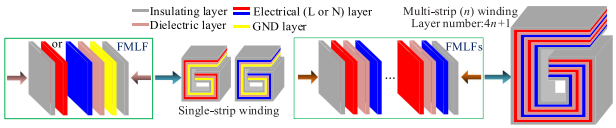

Fig. 2. Structure of the FMLF-based windings.

embedded in one of the windings, for producing CM capacitances through interaction with adjacent electrical and dielectric layers. Moreover, the proposed model can mitigate function coupling between the inductor and capacitor in this way.

The rest of this article is organized as follows. In Section II, the proposed integrated structure is presented, then modeling and analysis of the distributed model under CM and DM activation is conducted in Section III. Section IV provides the specification design principles, based on which, a prototype of the proposed EMI choke is built for experimental verification in Section V. Finally, Section VI concludes this article.

II. STRUCTURE OF THE PROPOSED EMI CHOKE

FMLFs are composed of electrical, dielectric, and insulating layers. Among them, electrical layers serve as the inductive windings that produce inductances, and the composition of electrical and dielectric layers is similar to a parallel capacitor; insulating layers provide insulation protection. Fig. 2 shows the FMLF-based single-strip and multistrip windings, which contain one and n (L or N layer number) groups of electrical layers, respectively. Multistrip FMLF-based windings are interleaved structures with $2n$ electrical layers and $(2n-1)$ dielectric layer. The equivalent lumped models of the single and multi-strip FMLF-based windings under different terminal activating modes can be concluded as shown in Table I (because CN1 and CN2 activating modes are enough for EMI choke design, so the other activating modes for different LC units are not presented here). In CN1 connection mode (three of the terminals are activated), the equivalent circuit of the winding is composed of a line inductor and a capacitor branch. In CN2 connection mode (the terminals are all activated), the equivalent unit consists of two full coupled line inductors and a capacitor connected between the two lines. It is worth mentioning that the activating mode and the FMLFs layer-number have a significant influence on the equivalent lumped inductance and capacitance, respectively. Compared with CN1 mode, the CN2 model can double the line inductance due to the nearly full magnetic coupling. Compared with single-strip FMLF winding, the multi-(n)-strip can enlarge the capacitance by $(2n-1)$ times.

As depicted in Fig. 3, two common single-strip FMLFs windings (Winding-1 and Winding-2) are employed in the integrated model proposed in [38]. Both the windings are in CN1 activating mode, one is designed for integration of L-line inductor and L-to-ground capacitor, another is designed for integration of N-line inductor and N-to-ground capacitor. With such terminal (a_1-d_1 and a_2-d_2) configuration and connection, it can realize the integration design of a CM inductor and two CM capacitors based on a UU-core. In the lumped equivalent circuit, L_{CM1} (or C_{CM1}) and L_{CM2} (or C_{CM2}) denote the self-inductances (or CM capacitances) generated by Winding-1 and Winding-2, respectively. There is a nearly full coupling between L_{CM1} and L_{CM2}, which prompts them to constitute the CM inductor together. In addition, the leakage inductances of the CM windings in L and

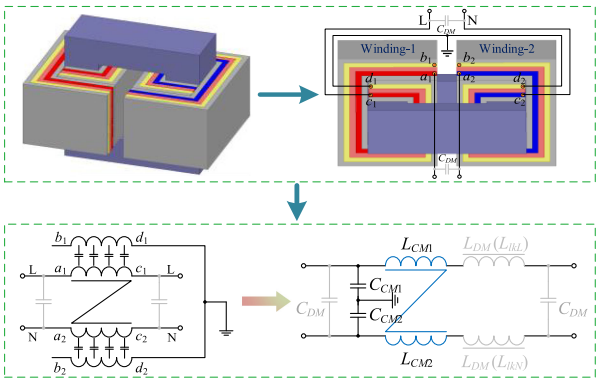

Fig. 3. Structure and lumped equivalent circuit of the existing integrated CM choke based on single-strip FMLF windings.

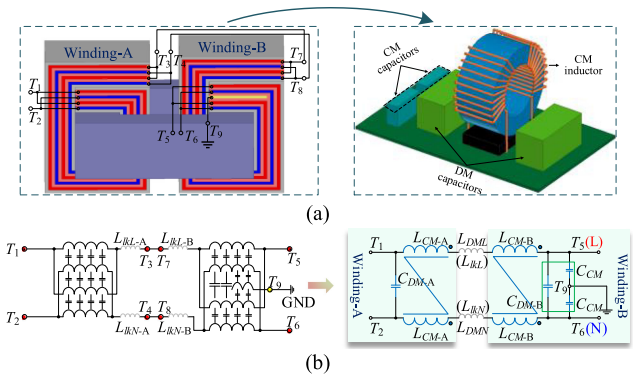

Fig. 4. Model of the proposed integrated EMI choke based on multistrip FMLF windings. (a) Structure. (b) Lumped equivalent circuit.

N lines (L_{lkL} and L_{lkN}) are utilized as DM inductances. In this condition, the DM noise attenuation is quite limited and out of control. Hence, if required, discrete DM capacitors generally need to be extra-designed, which will degrade the integration level.

With a magnetic core of the same geometry, the proposed structure of a fully integrated EMI choke is presented in Fig. 4(a), which is built based on two multistrip FMLF windings: 1) Winding-A and 2) Winding-B, in CN2 connection mode. Slightly different from Winding-A, there is a certain length of the conductive layer used as the GND connector embedded in the middle of Winding-B. There are nine terminals (T_1-T_9) in the whole model, which are connected in common mode. In theory, through this configuration, the electrical layers still act as CM windings, the main capacitances produced between L and N layers can be utilized as DM capacitances. Moreover, CM capacitances can be generated due to interaction between the embedded GND and adjacent L/N layers. In addition, the leakage inductances of the CM windings under DM activation are also employed as DM inductances. In this way, the model can integrate all the CM and DM filtering elements. As shown in Fig. 4(b), the full electromagnetic integration of an EMI filter can be realized. Where $L_{\text{CM-A}}$ and $L_{\text{CM-B}}$ denote the self-inductances in L or N line produced by Winding-A and Winding-B, respectively; C_{CM} is the achieved CM inductance in Winding-B; L_{DML} and L_{DMN} represent the equivalent leakage

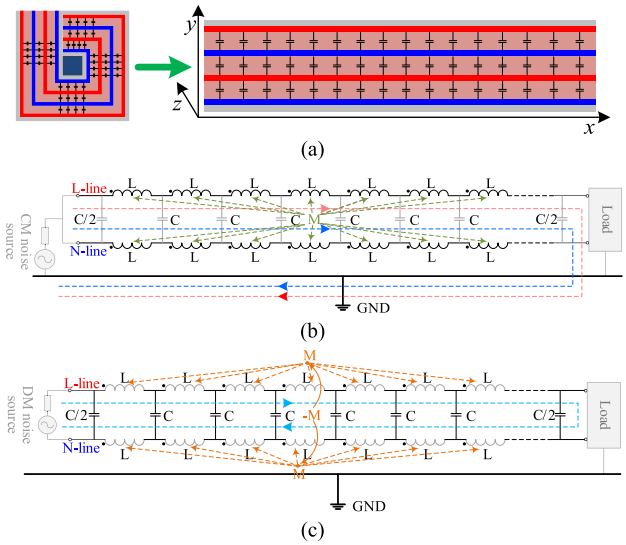

Fig. 5. Outspread structure and electromagnetic features of a one-turn multistrip FMLFs winding. (a) Outspread description. The coupling states under (b) CM excitations and (c) DM excitations.

inductances in L and N lines, respectively; $C_{\text{DM-A}}$ and $C_{\text{DM-B}}$ stand for the equivalent DM capacitances generated by Winding-A and Winding-B, respectively.

III. Modeling and Analysis of the Proposed Model

A. Distributed Model

For clearly presenting the distributed electromagnetic circuit (DEMC) of the FMLFs winding, the parameters are assumed to be evenly distributed along the direction of the z-axis. Therefore, it can be analyzed and discussed in a simplified 2-D model. In [38], the single-strip FMLFs windings used for a CM choke design have been analyzed in detail, it will not be repeated here. This section is mainly focused on the multistrip windings utilized in the proposed model. As depicted in Fig. 5, to make it easier to further understand, the analysis is begun with a one-turn FMLFs winding, Fig. 5(a) presents its 2-D outspread structure. With the performance of the core, the coupling states under CM and DM excitations are depicted in Fig. 5(b) and (c), respectively, L and C denote the LC cascade structure of each distributed section; M represents the mutual inductance among different sections. From which the following can be seen.

1) Under CM excitations, the capacitance generated between L and N layers will be out of operation and there is a nearly full positive coupling between the inductances in L and N layers.
2) Under DM excitations, the capacitance is activated, but there is a nearly full negative coupling between the inductances in L and N layers.

Therefore, Winding-A can be regarded as a function-decoupled integration unit of a CM inductor and a DM capacitor.

For a further comprehensive analysis, as presented in Fig. 6, a two-turn Winding-B is discussed. Fig. 6(a) shows its outspread structure, where C_{na} and C_{nc} (n = 1, 2, 3, 4) stand for the capacitances produced by the corresponding windings in the

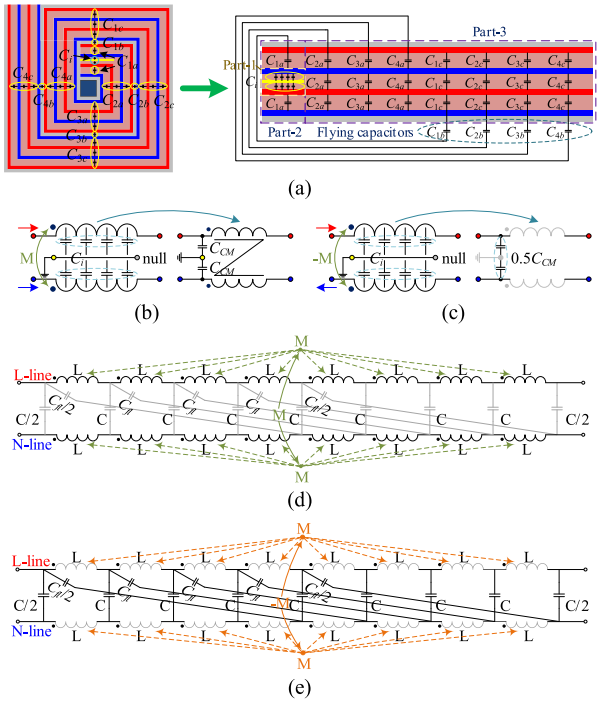

Fig. 6. Outspread structure and electromagnetic features of a two-turn winding-B. (a) Whole outspread description. The states of Part-1 under (b) CM and (c) DM excitations. The coupling states of the whole winding under (d) CM and (e) DM excitations.

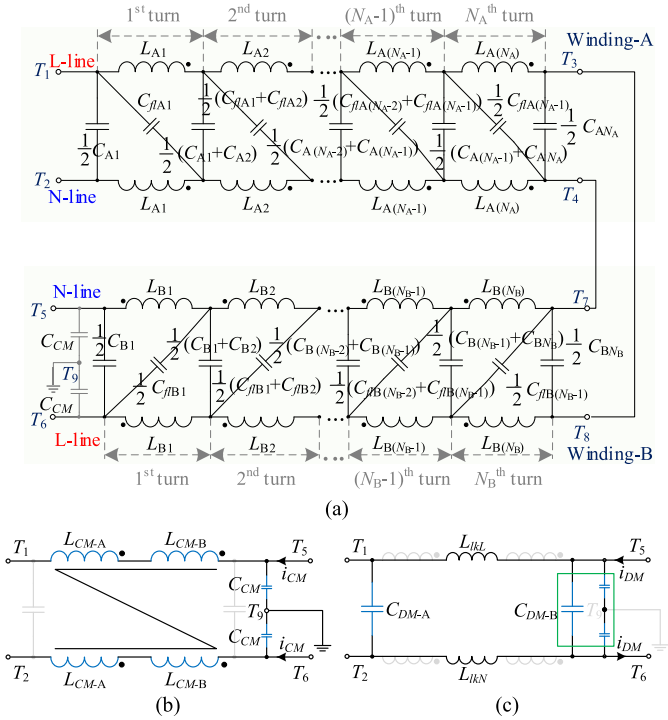

Fig. 7. Circuit model of the whole designed EMI choke. (a) DEMC model. (b) Equivalent CM circuit. (c) Equivalent DM circuit.

first and second turns, respectively; C_i represents the generated capacitance connected from L or N layer to the GND layer in Part-1. Actually, there will be some flying capacitors formed when the winding has multiturns, which are indicated as $C_{n\mathrm{b}}$. Regarding Part-1, the terminals are under low-pass *LC* filter configuration [29], it is mainly designed to produce extra CM capacitances. As shown in Fig. 6(b), Part-1 can be seen as a submodule composed of a CM inductor and two CM capacitors (combination of two *LC* modules) under CM excitations. However, under DM excitations, the inductances generated in L- and N-line will counteract each other. Thus, as presented in Fig. 6(c), the equivalent circuit is a DM capacitor with its capacitance $= 0.5\,C_{\mathrm{CM}}$. On the whole, compared with a common multistrip winding, Winding-B has no significant difference in the CM inductance and DM capacitances, except for the extra CM capacitances. If both windings have the same turn number, their CM inductances and DM capacitances approximately meet the following relationship:

$$\begin{cases} L_{\mathrm{CM-A}} = L_{\mathrm{CM-B}} \\ C_{\mathrm{DM-B}} = C_{\mathrm{DM-A}} - 0.5C_{\mathrm{CM}} \approx C_{\mathrm{DM-A}}. \end{cases} \tag{1}$$

Based on the analysis above, for an integral analysis, the entire Winding-B can be approximately regarded as a common multistrip winding. The CM and DM coupling states are depicted in Fig. 6(d) and (e), respectively. The distribution of inductances and capacitances is similar to those of a one-turn multistrip winding. But it is worth mentioning that flying capacitors will be produced between two adjacent FMLF coils through the insulating layer, which is uniformly named C_{fl} in the DEMC. It can be observed that flying capacitors are distributed between L and N lines, which exist in differential mode. However, due to the much greater thickness and lower permittivity of insulating layers, flying capacitances are much smaller than the dominant DM capacitances. Therefore, they can be neglected during the design procedure. Taking each turn as a subunit, the DEMC model of the entire EMI choke can be depicted in Fig. 7(a). Where $L_{\mathrm{A}n}$($C_{\mathrm{A}n}$ or $C_{fl\mathrm{A}n}$) and $L_{\mathrm{B}n}$($C_{\mathrm{B}n}$ or $C_{fl\mathrm{B}n}$) denote the self-inductance, capacitance, and flying capacitance in each turn of Winding-A and Winding-B, respectively. $n = 1, 2, \ldots, N_{\mathrm{A}}$ or N_{B}, N_{A}, and N_{B} represent the turn numbers of the windings. It should be noted that there are corresponding positive and negative couplings between Winding-A and Winding-B with different activation. From the theoretical analysis above, the lumped equivalent circuits under CM and DM excitations can be simplified in Fig. 7(b) and (c), respectively. Compared with the existing CM choke, the proposed EMI choke can integrate two independent DM capacitances, which will upgrade the DM filtering circuit, then increase the whole DM noise attenuation.

B. Analysis of Magnetic Circuits

Fig. 8 shows the equivalent magnetic circuits of the proposed EMI choke, for comparison, the existing CM choke is introduced first. It has been mentioned that the existing CM choke is designed with two single-strip windings, whose L and N layers are located in Winding-1 and Winding-2, respectively. Thus, its equivalent CM and DM magnetic circuits can be such depicted in Fig. 8(a) and (b), where R_{cu}(or R_{cl}) stands for the reluctance of the upper(or lower) U-core. $\Phi_{\mathrm{W1\text{-}CM}}$(or $\Phi_{\mathrm{W1\text{-}DM}}$)

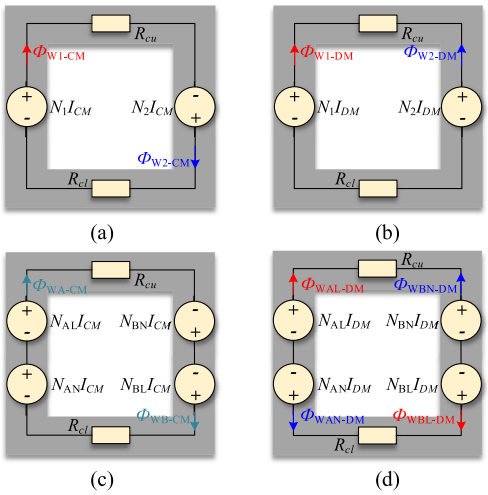

Fig. 8. Equivalent magnetic circuits: The existing CM choke under (a) CM and (b) DM excitations. The proposed EMI choke under (c) CM and (d) DM excitations.

and $\Phi_{\text{W2-CM}}$(or $\Phi_{\text{W2-DM}}$) are the fluxes produced by Winding-1 and Winding-2, respectively, Under CM(or DM) excitations. It can be seen that the fluxes produced by both windings will strengthen each other under CM excitations, and the coupling coefficient is close to 1 in such a UU-core. In contrast, the status under DM excitations is opposite, the fluxes generated by L and N layers will neutralize each other. However, in the proposed EMI choke, both L and N layers are included in each of the multistrip windings, this structure will lead to a different coupling effect. Its equivalent CM and DM magnetic circuits are presented in Fig. 8(c) and (d), respectively, where $\Phi_{\text{WA-CM}}$ (or $\Phi_{\text{WB-CM}}$) denotes the CM flux produced by Winding-A(or Winding-B); $\Phi_{\text{WAL-DM}}$(or $\Phi_{\text{WAN-DM}}$) and $\Phi_{\text{WBL-DM}}$(or $\Phi_{\text{WBN-DM}}$) represent the DM fluxes generated by L-layer(or N-layer) in Winding-A and Winding-B, respectively. Similar to the CM choke model mentioned above, the generated individual flux will strengthen each other under CM excitations. Moreover, the proposed model is actually equivalent to a structure with L and N lines wound in parallel. Therefore, its CM inductance is four times as much as that of the existing CM choke in theory, if windings of both chokes have the same turn number. As for the DM coupling status, as shown in Fig. 8(d), the fluxes produced by L and N layer windings will also counteract each other.

On the other hand, the leakage inductance of such designed windings will have a difference. A brief comparison of leakage paths in the existing and proposed models under DM excitations is presented in Fig. 9. In the existing CM choke, the main leakage paths are provided by side-legs of the core and surrounding air. But in the interleaved multistrip windings of the EMI choke, leakage fluxes generated by L and N layers will neutralize each other when they flow through side-legs of the core. Only a few leakage fluxes have no intersection, as those may pass between the odd and even electrical layers. Hence, in theory, the existing CM choke can obtain a much greater leakage inductance compared to the proposed EMI choke. But meanwhile, it will result in more serious radiated emissions.

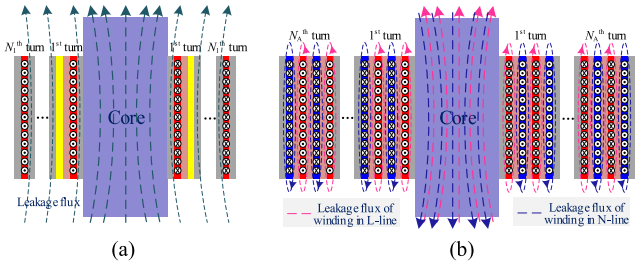

Fig. 9. Leakage paths of (a) existing CM choke and (b) proposed EMI choke under DM excitations.

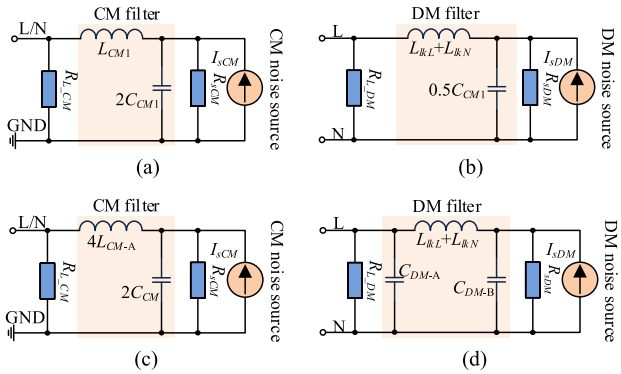

Fig. 10. Equivalent simplified filtering circuits. (a) CM and (b) DM of the existing CM choke. (c) CM and (d) DM of the proposed EMI choke.

IV. Design Principles

According to the analysis above, the equivalent CM and DM filtering circuits of different electromagnetic integrated chokes can be simplified as Fig. 10. In practical design, both applied windings are symmetrical ($N_1 = N_2$, $N_{\text{A}} = N_{\text{B}}$), thus, in the existing CM choke, $L_{\text{CM1}} = L_{\text{CM2}}$, $C_{\text{CM1}} = C_{\text{CM2}}$; in the proposed EMI choke, $L_{\text{CM-A}} = L_{\text{CM-B}}$, $C_{\text{DM-A}} \approx C_{\text{DM-B}}$. It can be observed that the lumped CM circuits of both chokes are LC low-pass (Γ-type) filters. However, the lumped DM circuits are Γ-type and π-type (CLC) filters, respectively, as shown in Fig. 10(b) and (d).

From the filtering circuits, CM and DM IL expressions of the proposed EMI choke can be derived as (2), where L_{CM} and L_{DM} represent the equivalent CM and DM inductances, respectively; $L_{\text{DM}} = L_{lkL} + L_{lkN}$; $C_{\text{DM}} = C_{\text{DM-A}} = C_{\text{DM-B}}$. From [18], the required cut-off frequencies of CM and DM filtering circuit ($f_{c,\text{CM-req}}$ and $f_{c,\text{DM-req}}$) can be obtained from (3). Then, the expected values of L_{CM}, C_{CM}, and C_{DM} can be specified according to (4), where $A_{\text{CM-req}}$ and $A_{\text{DM-req}}$ stand for the required CM and DM attenuation (in decibel), respectively, at f_{T} (the frequencies with exceeding EMI levels). It is necessary to be indicated that L_{CM} is generally determined based on a preselected C_{CM} subjected to leakage constraint. As for the DM components, it is hard to predesign the parameters efficiently due to the unpredictable leakage inductance in such a model. The leakage of a traditional toroidal CM choke is commonly in the range: $(0.1\sim2)\% \times L_{\text{CM}}$ from practical experience [4]. In this article, DM capacitances are predesigned with the leakage

assumed to be $0.1\% \times L_{\mathrm{CM}}$

$$\begin{cases} G_{\mathrm{CM}}(s) = 2L_{\mathrm{CM}}C_{CM}s^2 + 2R_{L\_\mathrm{CM}}C_{\mathrm{CM}}s + 1 \\ G_{\mathrm{DM}}(s) = L_{\mathrm{DM}}C_{\mathrm{DM}}^2R_{L\_\mathrm{DM}}s^3 + L_{\mathrm{DM}}C_{\mathrm{DM}}s^2 \\ \qquad\qquad +2R_{L\_\mathrm{DM}}C_{\mathrm{DM}}s + 1 \end{cases} \tag{2}$$

$$\begin{cases} f_{c,\mathrm{CM-req}} \le \min\left(f_T \times 10^{-\frac{A_{\mathrm{CM-req}}}{40}}\right) \\ f_{c,\mathrm{DM-req}} \le \min\left(f_T \times 10^{-\frac{A_{\mathrm{DM-req}}}{60}}\right) \end{cases} \tag{3}$$

$$\begin{cases} f_{c,\mathrm{CM}} \approx \frac{1}{2\pi}\sqrt{\frac{1}{2L_{\mathrm{CM}}C_{\mathrm{CM}}}} \\ f_{c,\mathrm{DM}} = \frac{1}{2\pi}\sqrt[3]{\frac{1}{L_{\mathrm{DM}}C_{\mathrm{DM}}^2R_{L\_\mathrm{DM}}}}. \end{cases} \tag{4}$$

In a practical fully integrated EMI choke, L_{CM} is determined from (5), where $R_{\mathrm{c\text{-}eq}}$, $A_{\mathrm{c\text{-}eq}}$, and $l_{\mathrm{c\text{-}eq}}$ denote the equivalent reluctance, cross-sectional area, and length of the UU-core, respectively; μ_0 and μ_{r} represent the permeability of the vacuum and core, respectively

$$\begin{aligned} L_{\mathrm{CM}} &= L_{\mathrm{CM}L} \parallel L_{\mathrm{CM}N} = N_{\mathrm{A}} \cdot \frac{\Phi_{\mathrm{WA}}+\Phi_{\mathrm{WB}}}{i_{\mathrm{CM}}} \\ &= \frac{4N_{\mathrm{A}}^2}{R_{\mathrm{c-eq}}} = \frac{4N_{\mathrm{A}}^2\mu_0\mu_r A_{\mathrm{c-eq}}}{l_{\mathrm{c-eq}}} \end{aligned}\Bigg|_{\mu_0 = 4\pi\times10^{-7}\mathrm{H/m}} \tag{5}$$

$$\begin{cases} C_{\mathrm{CM}} = \frac{\varepsilon_r\varepsilon_0 A_G}{d_d} = \frac{\varepsilon_r\varepsilon_0 l_G w_e}{d_d} \\ C_{\mathrm{DM}} = (2n-1)\times\frac{\varepsilon_r\varepsilon_0 A_e}{d_d} = \frac{3\varepsilon_r\varepsilon_0 l_t w_e}{d_d} \end{cases}\Bigg|_{\varepsilon_0 = 8.85\times10^{-12}\mathrm{F/m}}. \tag{6}$$

It is worth mentioning that the formation principle of the integrated capacitances is similar to parallel plate capacitors, thus, C_{CM} and C_{DM} can be estimated from (6), where ε_0 and ε_r stand for the permittivity of vacuum and dielectric layer; A_G and A_e denote the mapping areas of GND-layer and electrical layer, respectively, in the xz-plane; l_t and l_G stand for the length of the total winding and embedded GND layer, respectively; w_e denotes the width of the electrical layer, and d_d represents the thickness of the dielectric layer.

When the core candidate is selected, the realized CM inductance only rests with the turn number N_{A}(or N_{B}). As for capacitances, they involve a problem of the multidimensional parameter design. Based on the selected dielectric material, the attained CM capacitance depends on l_G, w_e, and d_d, the DM capacitance is determined by l_t, w_e, and d_d. In addition, it is evident that l_t is closely related to the core size, layer thickness, and turn number of the winding. l_t can be estimated from

$$l_t = \sum_{N=1}^{N_{\mathrm{A}}} 4w \approx 4\left[\sum_{N=1}^{N_{\mathrm{A}}}\left[C + 2(N-1)(2d_i + 4d_e + 3d_d)\right]\right] \tag{7}$$

where C stands for the width of the core leg, as indicated in the core structure below; d_i and d_e denote the thickness of the insulating and electrical layers, respectively.

On the other hand, the reasonability of the selected UU-type core size is another main factor for the design of the proposed EMI choke. In this article, the expected utility ratio of the core window is above a certain level for guiding this selection. As presented in Fig. 11, the utility ratio has two indices: r_x (in the x-axis) and r_z (in the z-axis), respectively, which are relevant to the total thickness (d_t) and height (h_w) of the winding. In order to take full advantage of the core window, while reserving a space margin for the manufacture, the utility ratio of the core window is limited as

$$\begin{cases} 60\% \le r_x = \frac{2d_t}{E} = \frac{2\times N_{\mathrm{A}}(d_i + d_e + d_d)}{E} \times 100\% \le 90\% \\ 60\% \le r_z = \frac{h_w}{2\times(B-D)} \times 100\%. \end{cases} \tag{8}$$

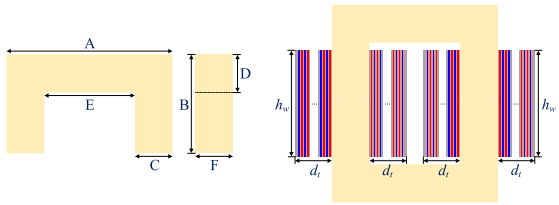

Fig. 11. Core specifications.

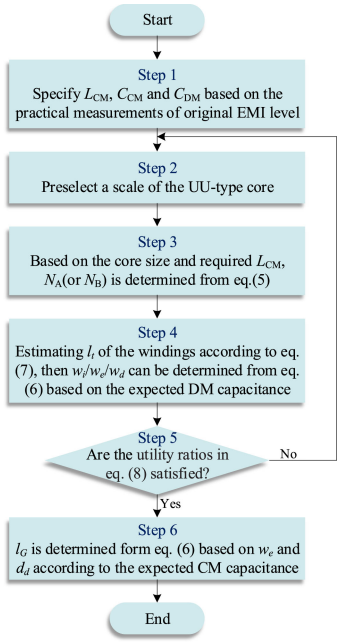

Fig. 12. Design procedure of the proposed EMI choke.

The presentation above has detailed the complete parameter design procedure of the proposed EMI choke. In a practical design, the core type can be preselected based on engineering experiences (considering the power level, effective frequency band, and cost). Then, choosing an appropriate core scale, which can meet the limited utility ratio with the designed windings for attaining the required filtering inductances and capacitances. The clearer procedure can be depicted as the flow diagram shown in Fig. 12. From this, the proposed full integrated EMI choke can be reasonably designed in practical applications.

V. Implementation and Verification

In this section, a 200-W/50-Hz SiC-MOSFET inverter is utilized as the experimental platform, as shown in Fig. 13, the switching

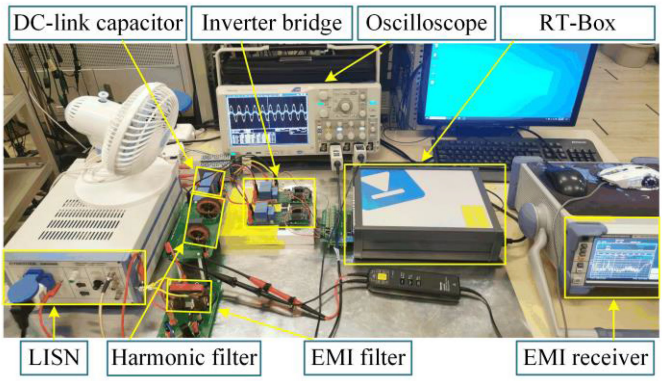

Fig. 13. Schematic diagram of the experimental platform.

TABLE II
CHARACTERISTICS OF COMMONLY USED DIELECTRIC FILMS

Parameters	Materials (High Polymer)		
	Polypropylene (PP)	Polyphenylene Sulfide (PPS)	Polyimide (PI)
Relative permittivity (ε_r)	2.2	3.0	3.5
breakdown voltage (V/μm)	200~400	180	280
Maximum operating temperature (°C)	80~105	130~140	≥500

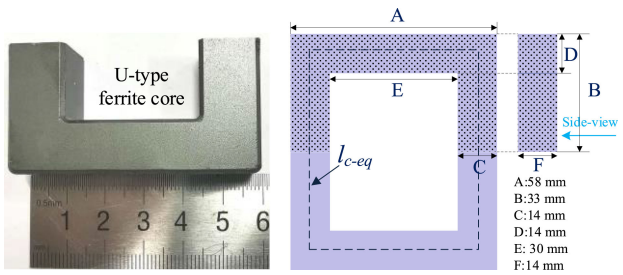

Fig. 14. Size of the selected UU-core.

frequency is 200 kHz based on the bipolar sinusoidal pulsewidth modulation (SPWM) technique.

According to the original measured CM and DM EMI noise levels, the expected $L_{\rm CM}$, $C_{\rm CM}$, and $C_{\rm DM}$ are 3.0 mH, 5400 pF, and 56 nF, respectively. There are some types of dielectric films available on the market, such as the widely used polypropylene (PP), polyphenylene sulfide (PPS), and polyimide (PI). It can be seen from the comparison in Table II that PI films have better comprehensive properties, especially the greater permittivity and higher tolerable temperature. In this article, PI films are utilized for the EMI choke design. Considering the feasibility of the materials in manufacture from practical experience, the thicknesses of electrical and dielectric layers are preselected to be 50 μm. In addition, the thickness of the insulating layer is 0.13 mm. All the materials are directly available on the market.

Based on the expected designed filter parameters and preselected thicknesses of the films, the UU-58/33/14 PC40 ferrite core is selected according to Section IV, its size is provided in Fig. 14. From the datasheet, μ_r, $A_{\text{c-eq}}$, and $l_{\text{c-eq}}$ of the core are 2300 (@23 °C), 192 mm, and 196 mm^2. Fig. 15 shows

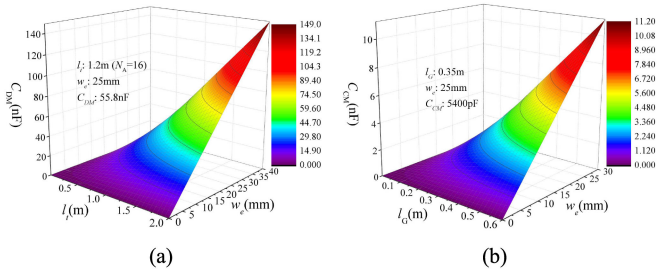

Fig. 15. Distributed chart among $w_{\rm d}$, $l_{\rm G}$, $l_{\rm T}$, and (a) $C_{\rm DM}$ or (b) $C_{\rm CM}$.

TABLE III
PARAMETER DESIGN OF THE INTEGRATED EMI CHOKES

Type of the filter	Parameters				
	N_1 or $N_{\rm A}$	$l_{\rm G}$	$L_{\text{CM-eq}}$	$C_{\rm CM}$	$C_{\rm DM}$
Existing model	32	0.35m	3.0mH	5400pF	-
Proposed model	16	0.35m	3.0mH	5400pF	56nF

the distributed charts of $C_{\rm DM}$ and $C_{\rm CM}$ with different l_t, l_G, and w_e. First, from (5), $N_{\rm A}$ is determined to be 16, then the estimated required l_t is about 1.2 m from (9). Finally, it can be observed from Fig. 15(a) that w_e should be at least 25 mm to meet the requirement of $C_{\rm DM}$. Moreover, as shown in Fig. 15(b) l_G should be at least 0.35 m to satisfy the required $C_{\rm CM}$ if $w_e =$ 25 mm. Therefore, in this article, w_i, w_e, and w_d are designed to be 30, 25, and 26 mm, respectively. It is worth mentioning that w_d is slightly greater than w_e for providing a 1-mm space margin to prevent short circuit, and w_i is adjusted to be greater to ensure insulation between adjacent L and N layers. In addition, the existing-model-based CM choke is built for comparison. Both chokes are designed with the same materials, the designed parameters are listed in Table III, both chokes have the same expected CM filter parameters. It should be noted that N_1 is double $N_{\rm A}$ for obtaining the same CM inductance from the analysis in Section III. In this design, utility ratios of the core window are about 65.1%(r_x) and 78.9%(r_z) according to (8), which meet the limitations set in advance

$$l_t = \sum_{N=1}^{N_{\rm A}} 4w \approx 4\left[\sum_{N=1}^{N_{\rm A}} \left[14\text{mm} + 2\left(N-1\right) \times 0.61\,\text{mm}\right]\right]. \tag{9}$$

Fig. 16 shows the output waveforms of the inverter system with 200-W load, the ac side voltage and current are 200 V and 2 A (peak value), respectively. Under such a current excitation, the distributions flux density of the designed CM and EMI chokes are presented in Fig. 17. It indicates that leakage fluxes of the EMI choke are much less than those of the CM choke, which is in accord with the theoretical analysis. Actually, this feature will lead to a smaller DM inductance, but less radiated emissions, it will be further validated in the following contents.

Prototypes of the existing CM choke and the proposed EMI choke are built for a practical comparison, as presented in Fig. 18(a) and (b), respectively. From Fig. 19, it can be seen that there are no significant differences in weight and volume of the two chokes although the proposed EMI choke integrates

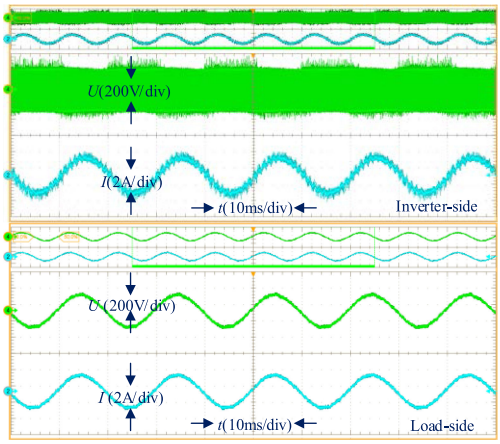

Fig. 16. Output waveforms of the inverter system.

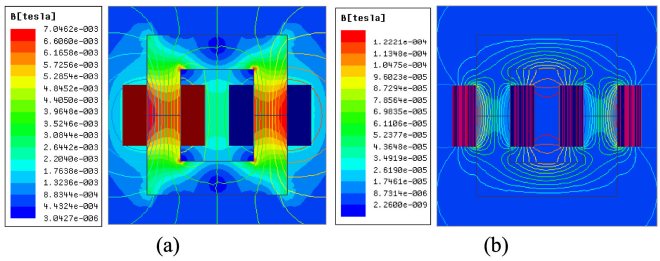

Fig. 17. Distributions of magnetic flux density in the (a) CM choke and (b) EMI choke under the DM current excitation.

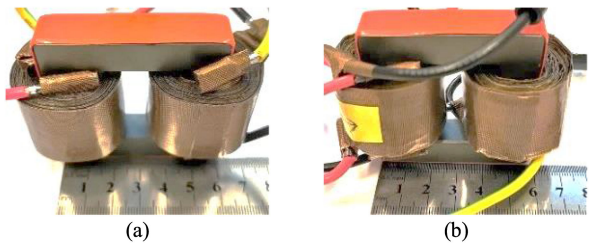

Fig. 18. Prototypes of the designed (a) CM choke and (b) EMI choke.

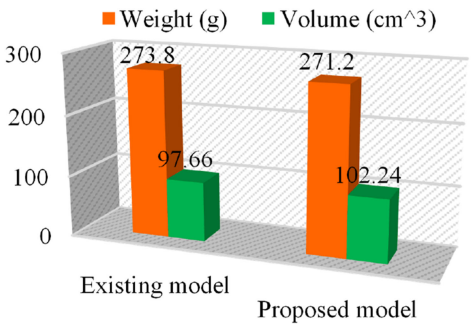

Fig. 19. Weight and size comparisons between the CM and EMI chokes.

extra DM capacitances. The weights of the CM and EMI chokes are 273.8 and 271.2 g, respectively. And the volume of the EMI choke is slightly greater than that of the CM choke, which is about 102.2 and 97.7 g, respectively.

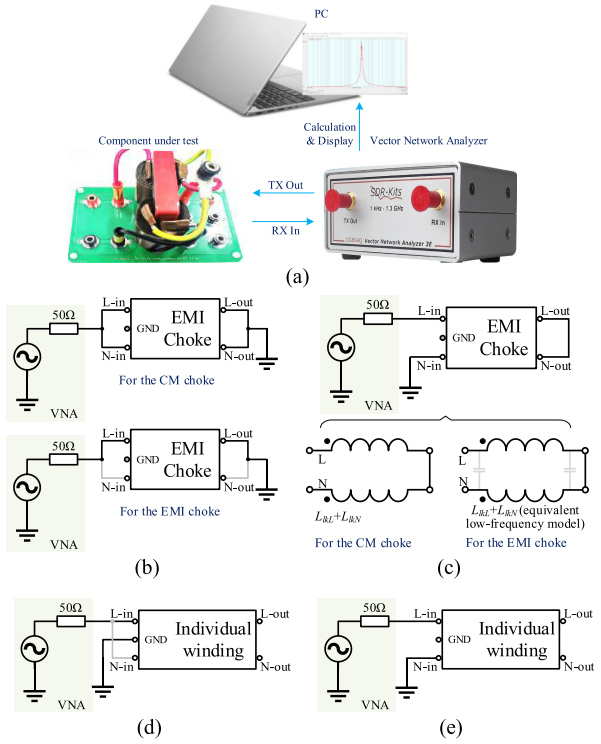

Fig. 20. (a) Experimental configurations to measure the impedances of (b) CM inductance, (c) DM inductance, (d) CM capacitance, and (e) DM capacitance.

Furthermore, a vector network analyzer (VNA) is used to get the impedance characteristics of different filtering components. The test platform with signal-flow indications is shown in Fig. 20(a), there are some differences in terminal configurations of the CM and EMI chokes due to different winding structures. For the proposed EMI choke, because the self-inductance produced by the windings in L-layer or N-layer is equal to its equivalent CM inductance, thus the self-inductance in L- or N-layer is measured to reflect the CM inductance, which can avoid the disturbance of DM capacitances with the two-port network configuration. As for the CM choke, there are no interfering factors with the two-port network configuration. Therefore, as shown in Fig. 20(b), the test configurations of CM inductances are set in such modes. Regarding the measurement of leakage (DM) inductance, as shown in Fig. 20(c), the terminal L-out is connected to N-out, then the measured inductance between L-in and N-in is actually the total leakage inductance. But for the proposed EMI choke, the high-frequency test result will be affected by the DM capacitances. The leakage inductance mainly dominates the low-frequency impedance performance, according to which it can be estimated. In contrast, the tests of capacitances are direct. As shown in Fig. 20(d) and (e), with L-out and N-out disconnected, L/N-in and GND terminals are activated for CM capacitance test; L-in and N-in terminals are configured for DM capacitance measurement.

Fig. 21 presents the impedance characteristics of different filtering components. As can be seen from Fig. 21(a) and (b), CM inductance and capacitance of both chokes have similar impedances over the range from 150 kHz to 30 MHz, which is

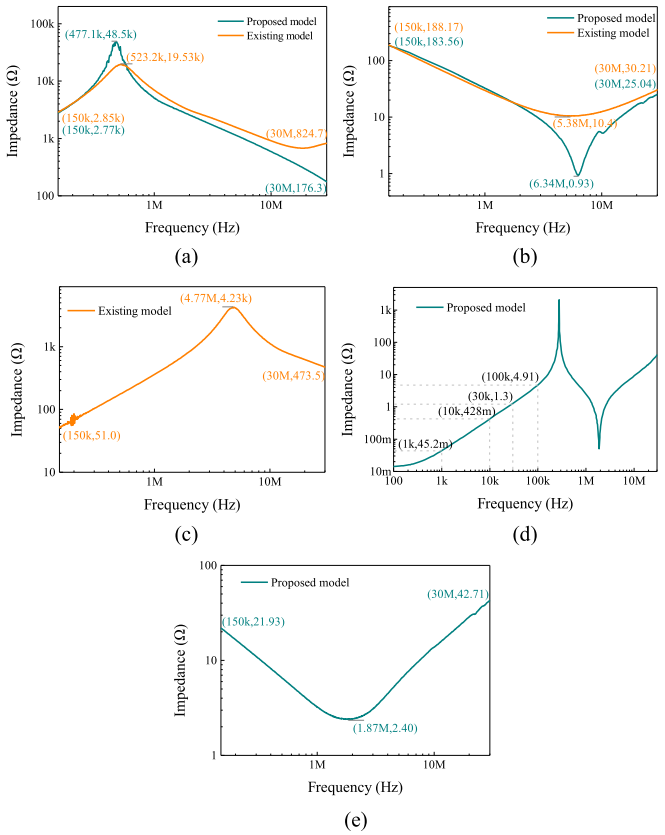

Fig. 21. Impedances of the filtering components. (a) CM inductances, (b) CM capacitances; DM inductances of the (c) CM and (d) EMI chokes; (e) DM capacitance of the EMI choke.

desired in this article. From Fig. 21(c) and (d), it is evident that the impedance of total leakage inductance of the CM choke is much larger than that of the EMI choke, this reflects a much greater leakage inductance of the CM choke. Moreover, Fig. 21(e) presents the DM capacitive impedance of the EMI choke, which shows satisfied low-impedance performance. It needs to be noted that the existing CM choke model is designed to integrate only CM inductor and CM capacitors, it has no capacity to integrate DM capacitance. So, actually, there is no independent DM capacitor in the designed CM choke. The DM capacitance that the choke can provide is equal to the equivalent capacitance of the CM capacitors in DM(0.5 C_{CM}).

Through practical measurements, the filtering parameters are provided in Table IV. It can be seen that the CM inductances or CM capacitances of both chokes are approximately equal. Compared to the expected value, the design errors of the CM inductances are about $+2.0\%$ and -1.0%, in the CM and EMI chokes, respectively. For CM capacitances, the corresponding errors are nearly -1.3% and $+4.5\%$. By contrast, the design error of the DM capacitance of the EMI choke is much greater, which is about -13.6%. Because DM capacitances depend on the design of the whole windings, which is hard to be perfectly realized during the hand-made process. In addition, there are no significant differences in parasitic parameters of CM filtering components of the two chokes. The EPCs of the CM inductors are 29.85 and 37.7 pF, and the ESLs of the CM capacitors are

TABLE IV
MEASURED PARAMETERS OF THE FILTERING COMPONENTS

Model type		EPC / ESR / L		C / ESR / ESL	
		L	EPC	C	ESL
Existing model	L_{CM}	3.06mH	29.85pF	—	—
	C_{CM}			5329pF	0.164 μH
	L_{DM}	53.6μH (L_{lkL}+L_{lkN})			
Proposed model	L_{CM}	2.97mH	37.7pF	—	—
	C_{CM}	—	—	5644pF	0.112 μH
	C_{DM}	—	—	48.4nF	0.150 μH
	L_{DM}	6.8μH (L_{lkL}+L_{lkN})			

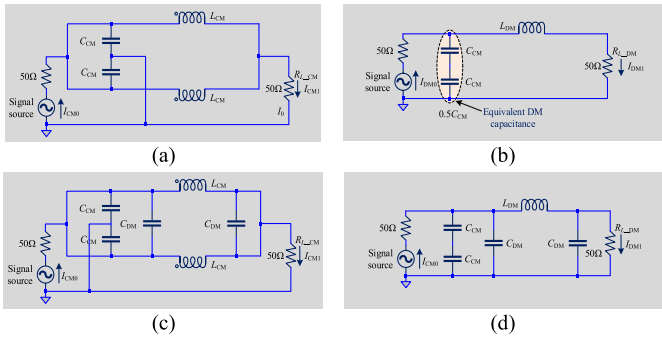

Fig. 22. Simulation configurations to measure (a) CM and (b) DM, ILs of the CM choke; (c) CM and (d) DM, ILs of the EMI choke.

0.164 and 0.112 μH, respectively, in the CM and EMI chokes. Here, it is worth to be noted that the parasitic inductor of a capacitor is mainly caused by the electrodes and down-lead. As for the parasitic inductance issue of a capacitor made by FMLFs winding, it can be ameliorated through decreasing the length of the down-lead of the terminals and area-scale of FMLFs. Thus, compared with single-strip FMLF windings, multistrip windings have the potential to reduce parasitic inductance, it is also a merit of multistrip FMLF windings. On the other hand, the total leakage inductance of the CM choke under DM excitations is nearly eight times as much as that of the EMI choke, the corresponding values are 53.6 and 6.8 μH. This result is in line with the theoretical analysis, which indicates the main drawback of the proposed model

$$IL_{(\mathrm{CM/DM})} = 10\lg\frac{P_{(\mathrm{CM0/DM0})}}{P_{(\mathrm{CM1/DM1})}} = 20\lg\frac{V_{(\mathrm{CM0/DM0})}}{V_{(\mathrm{CM1/DM1})}} = 20\lg\frac{I_{(\mathrm{CM0/DM0})}R_{L\_(\mathrm{CM/DM})}}{I_{(\mathrm{CM1/DM1})}R_{L\_(\mathrm{CM/DM})}} = 20\lg\frac{I_{(\mathrm{CM0/DM0})}}{I_{(\mathrm{CM1/DM1})}}. \tag{10}$$

Based on the lumped filtering circuits shown in Figs. 3 and 7, the CM and DM ILs of the CM and EMI chokes are measured using LT-Spice software with taking the parasitic parameters into account. The simulation configurations are presented in Fig. 22. It is well known that the IL of a filter is defined as the ratio of the load-side powers transmitted from the noise source without and with the filter, as expressed in (10), from which the CM and DM ILs can be obtained. As shown in Fig. 23(a), both chokes have similar CM ILs. The performance in a relatively low-frequency range is in accord with the expected ideal one. On the whole,

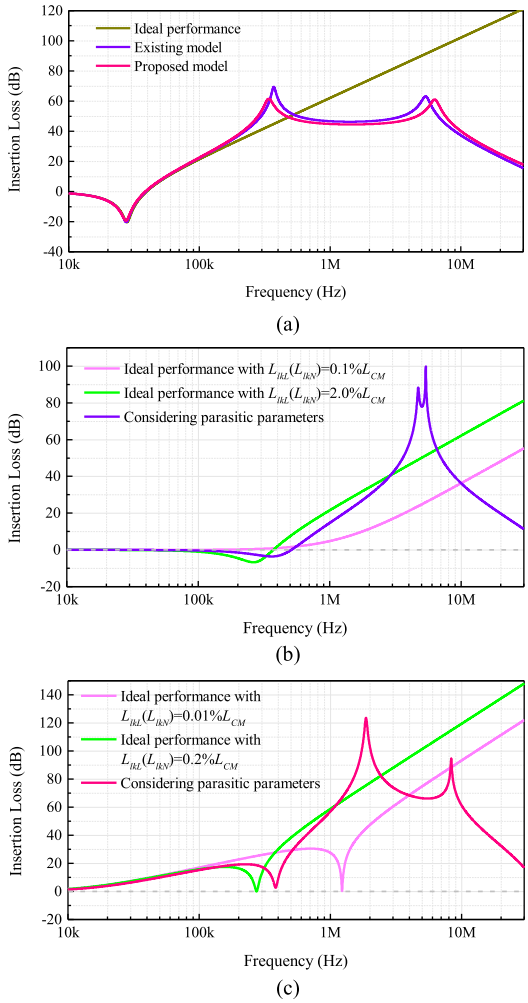

Fig. 23. ILs of the CM and EMI chokes. (a) CM ILs. DM ILs of the (b) CM and (c) EMI chokes.

the CM noise attenuation is satisfied though the high-frequency performance is degraded on account of the parasitic parameters. As for DM ILs, the DM attenuation of the CM choke mainly locates over the range from 1 to 20 MHz, as presented in Fig. 23(b). However, the attenuation over 10 MHz is decreased too much. What is worse, from 150 to 500 kHz, there will be a DM noise increment (within 10 dB) due to the resonance introduced by the *LC* unit. In comparison, as shown in Fig. 23(c), the state in the EMI choke is much better though the DM inductance is much less. From 150 to 500 kHz, the choke can provide a certain degree of DM noise attenuation, instead of amplification. In addition, the attenuation from 1 to 20 MHz is improved a lot but is also significantly reduced in the higher frequency range. The DM attenuation improvement of the proposed EMI choke mainly benefits from the following two aspects: 1) the extra integrated two DM capacitances; 2) the achieved high-order equivalent DM filtering circuit. Furthermore, the ILs have been directly measured using a two-port VNA, the relevant experimental configuration to measure CM a DM ILs are presented in Fig. 24(a) and (b), respectively. The measurement results of the CM ILs in Fig. 25(a) validate the same CM objective IL for both filters.

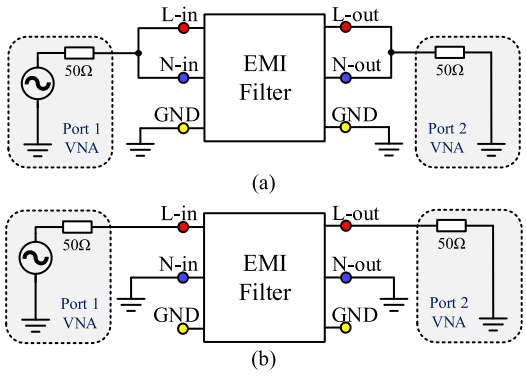

Fig. 24. Experimental configurations to measure (a) CM and (b) DM, ILs using a two-port VNA.

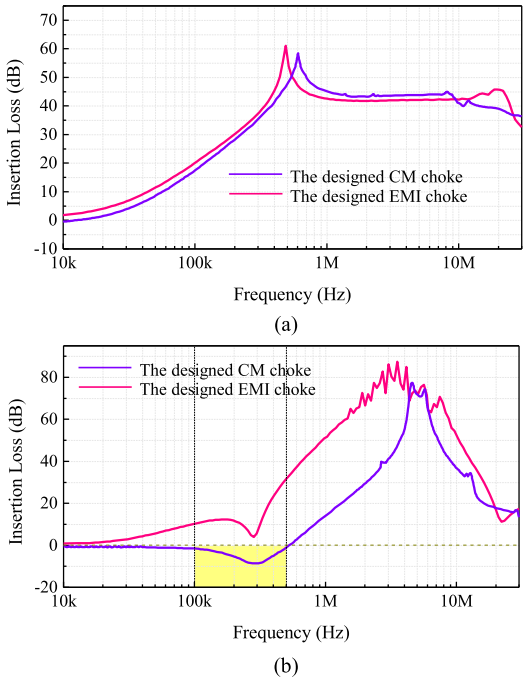

Fig. 25. Measured (a) CM and (b) DM ILs of the CM and EMI chokes.

Fig. 25(b) illustrates the DM ILs. By contrast, the proposed EMI choke has a better DM attenuation ability in the whole frequency range (150–30 MHz). In addition, it can be seen from Fig. 25(b) that the designed CM choke has negative performance from about 100 to 500 kHz, which will enlarge the noise by a certain degree (within 10 dB), but the proposed EMI choke can settle this issue. Moreover, although there are some differences in the high-frequency range between the ILs in simulation and experiment, the performances in relatively low-frequency are approximately consistent, it further reflects the validity of the lumped filtering models.

Finally, practical measurements of the ac-side conducted EMI noise of the inverter system are carried out, the circuit diagram of the whole system is clearly presented in Fig. 26. In this article, a two-line V-network LISN (made by Shenzhen Zhiyong Electronics Co., Ltd., part number: CYBERTEK EM5040B) with an embedded CM&DM separator is utilized to measure

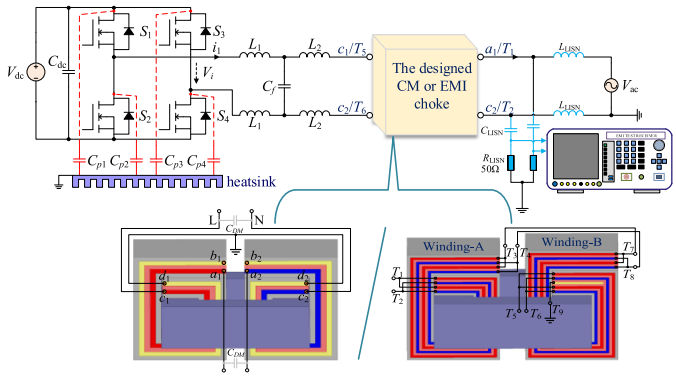

Fig. 26. Circuit diagram of the inverter system with the designed EMI filters.

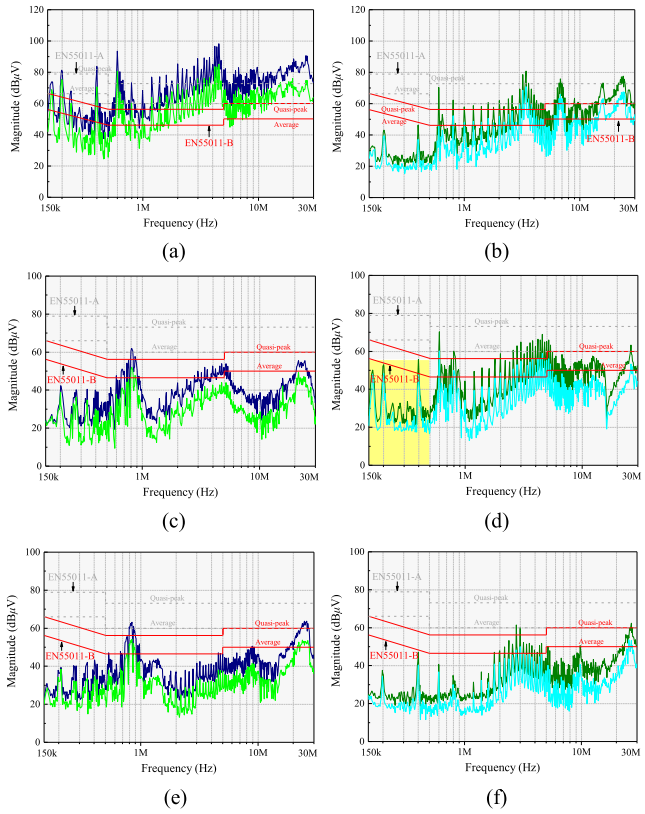

Fig. 27. Measurements of the conducted EMI noise of the inverter system in experiments. Without EMI filter: (a) CM and (b) DM; with the CM choke: (c) CM and (d) DM; with the EMI choke: (e) CM and (f) DM.

the CM and DM conducted emissions, standard EN55011-class B is referenced in the prototype design and experiments. As shown in Fig. 27(a) and (b), the original CM and DM EMI levels exceed the limitation to a great degree, especially the CM noise. The high-frequency DM noise has been mitigated by the prepositive harmonic filter. Fig. 27(c) and (d) shows the CM and DM EMI levels with the designed CM choke, respectively. As can be seen, the CM noise is reduced significantly, which roughly meets the standard. But the DM noise is unsatisfactory, it has been enlarged within 500 kHz, and the attenuation in high frequency is insufficient, which only meets the class-A limitation. By contrast from Fig. 27(c) and (e), both the CM and EMI chokes have similar CM noise mitigation abilities. However, from Fig. 27(f), it is worth mentioning that the DM noise suppression performance of the proposed EMI choke is much better than that of the CM choke, which is able to meet the requirement.

VI. Conclusion

In this article, the FMLF technique is further investigated; then, a fully integrated EMI choke model is proposed utilizing well-designed multistrip FMLFs windings. Compared with the existing single-strip FMLF-based integrated CM choke, the proposed one can realize the integration design of both CM and DM filters, meanwhile, almost without increasing the weight and size of the choke. Moreover, with similar CM attenuation, the proposed EMI choke has better DM noise suppression performance, which is validated through the test of the designed prototypes and practical EMI measurements of the objective system in experiments.

References

[1] B. Cougo, H. H. Sathler, R. Riva, V. D. Santos, N. Roux, and B. Sareni, "Characterization of low-inductance SiC module with integrated capacitors for aircraft applications requiring low losses and low EMI issues," *IEEE Trans. Power Electron.,* vol. 36, no. 7, pp. 8230–8242, Jul. 2021.

[2] M. Ardavan, C. W. Trueman, and K. A. Schmitt, "EMI risk assessment in a hospital ward with one and two roaming wireless transmitters," *IEEE Trans. Electromagn. Compat.,* vol. 57, no. 1, pp. 69–79, Feb. 2015.

[3] M. S. S. Nia, P. Shamsi, and M. Ferdowsi, "EMC modeling and conducted EMI analysis for a pulsed power generator system including an AC–DC–DC power supply," *IEEE Trans. Plasma Sci.,* vol. 48, no. 12, pp. 4250–4261, Dec. 2020.

[4] G. Ala, G. C. Giaconia, G. Giglia, M. C. D. Piazza, and G. Vitale, "Design and performance evaluation of a high power-density EMI filter for PWM inverter-fed induction-motor drives," *IEEE Trans. Ind. Appl.,* vol. 52, no. 3, pp. 2397–2404, May/Jun. 2016.

[5] G. Ala, M. C. D. Piazza, A. Ragusa, F. Viola, and G. Vitale, "EMI analysis in electrical drives under lightning surge conditions," *IEEE Trans. Electromagn. Compat.,* vol. 54, no. 4, pp. 850–859, Aug. 2012.

[6] *Industrial, Scientific and Medical Equipment, Radio-Frequency Disturbance Characteristics, Limits and Methods Of Measurement*, BS EN 55011 AMD 2, BSI Standards Ltd., 2018, pp. 1–10.

[7] H. Chung, S. Y. R. Hui, and K. K. Tse, "Reduction of power converter EMI emission using soft-switching technique," *IEEE Trans. Electromagn. Compat.,* vol. 40, no. 3, pp. 282–287, Aug. 1998.

[8] P. Lezynski, "Random modulation in inverters with respect to electromagnetic compatibility and power quality," *IEEE J. Emerg. Sel. Topics Power Electron.,* vol. 6, no. 2, pp. 782–790, Jun. 2018.

[9] D. Jiang, J. Chen, and Z. Shen, "Common mode EMI reduction through PWM methods for three-phase motor controller," *CES Trans. Elect. Mach. Syst.,* vol. 3, no. 2, pp. 133–142, 2019.

[10] M. Pahlevaninezhad, D. Hamza, and P. K. Jain, "An improved layout strategy for common-mode EMI suppression applicable to high-frequency planar transformers in high-power DC/DC converters used for electric vehicles," *IEEE Trans. Power Electron.,* vol. 29, no. 3, pp. 1211–1228, Mar. 2014.

[11] H. Li, Y. Zeng, B. Zhang, T. Q. Zheng, R. Hao, and Z. Yang, "An improved H5 topology with low common-mode current for transformerless PV grid-connected inverter," *IEEE Trans. Power Electron.,* vol. 34, no. 2, pp. 1254–1265, Feb. 2019.

[12] Y. Xiang, X. Pei, M. Wang, P. Shi, and Y. Kang, "An improved H8 topology for common-mode voltage reduction," *IEEE Trans. Power Electron.,* vol. 34, no. 6, pp. 5352–5361, Jun. 2019.

[13] S. Jiang and Y. Liu, "EMI noise reduction for the single-phase grid-connected inverter with a modified harmonic filter design," *IEEE Trans. Electromagn. Compat.,* vol. 63, no. 3, pp. 739–751, Jun. 2021.

[14] C. Wenjie, Y. Xu, and W. Zhaoan, "An active EMI filtering technique for improving passive filter low-frequency performance," *IEEE Trans. Electromagn. Compat.,* vol. 48, no. 1, pp. 172–177, Feb. 2006.

[15] B. Narayanasamy and F. Luo, "A survey of active EMI filters for conducted EMI noise reduction in power electronic converters," *IEEE Trans. Electromagn. Compat.,* vol. 61, no. 6, pp. 2040–2049, Dec. 2019.
[16] Y. Liu, S. Jiang, H. Wang, G. Wang, J. Yin, and J. Peng, "EMI filter design of single-phase SiC MOSFET inverter with extracted noise source impedance," *IEEE Electromagn. Compat. Mag.,* vol. 8, no. 1, pp. 45–53, Jan./Mar. 2019.
[17] R. Lai, Y. Maillet, F. Wang, S. Wang, R. Burgos, and D. Boroyevich, "An integrated EMI choke for differential-mode and common-mode noise suppression," *IEEE Trans. Power Electron.,* vol. 25, no. 3, pp. 539–544, Mar. 2010.
[18] Y. Liu, S. Jiang, W. Liang, H. Wang, and J. Peng, "Modeling and design of the magnetic integration of single- and multi-stage EMI filters," *IEEE Trans. Power Electron.,* vol. 35, no. 1, pp. 276–288, Jan. 2020.
[19] Y. Zhang, Z. Shen, and D. Jiang, "An integrated EMI filter scheme for paralleled inverter with zero-CM PWM algorithm," *IEEE J. Emerg. Sel. Topics Power Electron.,* vol. 9, no. 1, pp. 716–726, Feb. 2021.
[20] J. Borsalani, A. Dastfan, and J. Ghalibafan, "An integrated EMI choke with improved DM inductance," *IEEE Trans. Power Electron.,* vol. 36, no. 2, pp. 1646–1658, Feb. 2021.
[21] M. H. Hedayati and V. John, "Novel integrated CM inductor for single-phase power converters with reduced EMI," *IEEE Trans. Ind. Appl.,* vol. 53, no. 2, pp. 1300–1307, Mar./Apr. 2017.
[22] S. Jiang, Y. Liu, Z. Mei, J. Peng, and C. Lai, "A magnetic integrated LCL–EMI filter for a single-phase SiC-MOSFET grid-connected inverter," *IEEE J. Emerg. Sel. Topics Power Electron.,* vol. 8, no. 1, pp. 601–617, Mar. 2020.
[23] Z. Lingyin and J. D. van Wyk, "Frequency-domain modeling of integrated electromagnetic power passives by a generalized two-conductor transmission structure," *IEEE Trans. Circuits Syst. I, Reg. Papers,* vol. 51, no. 11, pp. 2325–2337, Nov. 2004.
[24] Z. Lingyin and J. D. van Wyk, "The modeling of planar multi-cell integrated reactive components based on multi-conductor generalized transmission structure theory," in *Proc. Conf. Rec. 37th IEEE IAS Annu. Meeting*, 2002, pp. 1787–1794.
[25] C. Rengang, J. D. van Wyk, S. Wang, and W. G. Odendaal, "Planar electromagnetic integration technologies for integrated EMI filters," in *Proc. IEEE Ind. Appl. Conf.*, 2003, pp. 1582–1588.
[26] S. Wang and C. Xu, "Design theory and implementation of a planar EMI filter based on annular integrated inductor–capacitor unit," *IEEE Trans. Power Electron.,* vol. 28, no. 3, pp. 1167–1176, Mar. 2013.
[27] C. Deng *et al.*, "Integration of both EMI filter and boost inductor for 1-kW PFC converter," *IEEE Trans. Power Electron.,* vol. 29, no. 11, pp. 5823–5834, Nov. 2014.
[28] X. Wu, Z. Wen, D. Xu, Y. Okuma, and K. Mino, "An integrating structure of EMI filter based on interleaved flexible multi-layer (FML) foils," in *Proc. IEEE Appl. Power Electron. Conf. Expo.*, 2009, pp. 491–497.
[29] J. Ma, W. Zhong, P. Chen, Y. Chen, and D. Xu, "An optimization design of output filter in a grid connected inverter with flexible multilayer foil technique," *IEEE Trans. Energy Convers.,* vol. 34, no. 1, pp. 221–231, Mar. 2019.
[30] C. Deng, S. Li, and J. Tang, "A review of flexible multilayer foil integration technology for passive components," *IEEE Trans. Power Electron.,* vol. 36, no. 11, pp. 13025–13038, Nov. 2021.
[31] C. Deng, T. Hao, and A. Escobar-Mejía, "An integrated passive device for quasi-resonant multiphase LED driver," in *Proc. IEEE Int. Power Electron. Motion Control Conf.*, 2020, pp. 2148–2153.
[32] C. Deng, Y. Yu, Y. Zhang, and A. Escobar-Mejía, "A novel passive integrated unit for a single-stage LED driver," in *Proc. IEEE Appl. Power Electron. Conf.*, 2020, pp. 2625–2630.
[33] C. Deng, Q. Jiang, A. Escobar-Mejía, and Y. Zhang, "A passive integrated unit for multi-channel SRC LED driver," in *Proc. IEEE Energy Convers. Congr. Expo.*, 2018, pp. 7032–7038.
[34] C. Deng, M. Yong, L. A. G. Rodriguez, J. C. Balda, and R. Li, "Passive integration using FMLF technique for integrated boost resonant converters," *IEEE Trans. Ind. Electron.,* vol. 67, no. 5, pp. 3756–3766, May 2020.
[35] C. Deng, J. Bo, and A. Escobar-Mejía, "A passive integration unit for current-feed single-switch resonant converter," in *Proc. IEEE Energy Convers. Congr. Expo.*, 2020, pp. 3478–3483.
[36] C. Deng, S. Li, and A. Escobar-Mejía, "A passive integration unit for single-phase three-level AC/DC resonant converter," in *Proc. IEEE Int. Power Electron. Motion Control Conf.*, 2020, pp. 2154–2160.
[37] J. Xiong, J. Jia, and C. Deng, "Passive integrations for Γ-Z source and DAB DC-AC bidirectional converter," in *Proc. IEEE Appl. Power Electron. Conf. Expo.*, 2019, pp. 650–655.
[38] X. Wu, D. Xu, Z. Wen, Y. Okuma, and K. Mino, "Design, modeling, and improvement of integrated EMI filter with flexible multilayer foils," *IEEE Trans. Power Electron.,* vol. 26, no. 5, pp. 1344–1354, May 2011.

Shiqi Jiang (Graduate Student Member, IEEE) received the B.S. degree in automation science from the Hubei University of Technology, Wuhan, China, in 2017, and the M.S. degree in control engineering from Shenzhen University, Shenzhen, China, in 2020. He is currently working toward the Ph.D. degree with the School of Electrical Engineering and Automation, Harbin Institute of Technology, Harbin, China.

His research interests include control technique, power integration, and EMI/EMC of the grid-connected inverters.

Wei Wang (Member, IEEE) received the B.S. degree in automatic test and control, the M.S. degree in electrical engineering, and the Ph.D. degree in mechanical electronic engineering from the Harbin Institute of Technology, Harbin, China, in 1984, 1990, and 2002, respectively.

Since 2003, she has been a Professor with the Department of Electrical Engineering, Harbin Institute of Technology. Her research interests include soft-switching converters, photovoltaic grid-connected inverters, and ac and dc microgrids.

Panbao Wang (Senior Member, IEEE) received the M.S. and Ph.D. degrees in electrical engineering from the Harbin Institute of Technology, Harbin, China, in 2011 and 2016, respectively.

In 2017, he joined the Department of Electrical Engineering, HIT, as an Assistant Professor. Since 2020, he has been an Associate Professor with the Department of Electrical Engineering, HIT. His research interests include distributed control and optimal operation of microgrids and highly integrated power electronics converters.

Dianguo Xu (Fellow, IEEE) received the B.S. degree in control engineering from Harbin Engineering University, Harbin, China, in 1982, and the M.S. and Ph.D. degrees in electrical engineering from the Harbin Institute of Technology (HIT), Harbin, China, in 1984 and 1989, respectively.

In 1984, he joined the Department of Electrical Engineering, HIT, as an Assistant Professor. Since 1994, he has been a Professor with the Department of Electrical Engineering, HIT. He was the Dean with the School of Electrical Engineering and Automation, HIT, from 2000 to 2010. And from 2014 to 2020, he was the Vice-President of HIT. He has authored/coauthored more than 1000 technical papers. His research interests include renewable energy generation technology, power quality mitigation, sensorless vector-controlled motor drives, and high-performance PMSM servosystem.

Prof. Xu is an Associate Editor for the IEEE TRANSACTIONS ON POWER ELECTRONICS, the IEEE TRANSACTIONS ON INDUSTRIAL ELECTRONICS, and the IEEE JOURNAL OF EMERGING AND SELECTED TOPICS IN POWER ELECTRONICS. He is the Chairman of IEEE Harbin Section. He is the recipient of the 2018 IEEE Industry Applications Society Outstanding Achievement Award.